Chemical Science

ROYAL SOCIETY OF CHEMISTRY

EDGE ARTICLE

View Article Online
View Journal

Check for updates

Cite this: DOI: 10.1039/d5sc08447d

All publication charges for this article have been paid for by the Royal Society of Chemistry

Simultaneous occupancy of $\mathrm{Cu_C}$ and $\mathrm{Cu_D}$ in the ammonia monooxygenase active site

Frank J. Tucci,[a] Madeline B. Ho,[a] Aaron A. B. Turner,[b] Lisa Y. Stein,[b] Brian M. Hoffman[a] and Amy C. Rosenzweig*[a]

Received 31st October 2025
Accepted 15th December 2025

DOI: 10.1039/d5sc08447d

rsc.li/chemical-science

Ammonia monooxygenase (AMO), a copper-dependent membrane enzyme, catalyzes the first and rate-limiting step of nitrification: the oxidation of ammonia to hydroxylamine. Despite its central role in the global nitrogen cycle and its biotechnological relevance, structural characterization of AMO has lagged behind that of its homolog, particulate methane monooxygenase (pMMO), due to the slow growth rates of ammonia-oxidizing bacteria and the instability of AMO upon purification. Recent cryoEM studies of *Nitrosomonas europaea* AMO and *Methylococcus capsulatus* (Bath) pMMO in native membranes revealed new structural features, including two adjacent copper-binding sites in the transmembrane region, $\mathrm{Cu_C}$ and $\mathrm{Cu_D}$, believed to constitute the active site. Although multiple structures were determined under various conditions, simultaneous occupancy of $\mathrm{Cu_C}$ and $\mathrm{Cu_D}$ was never observed, leaving their potential functional interplay unresolved. Here we report the 2.6 Å resolution cryoEM structure of AMO from *Nitrosospira briensis* C-128 in isolated native membranes. This structure reveals the first instance of simultaneous copper occupancy of the $\mathrm{Cu_C}$ and $\mathrm{Cu_D}$ sites, along with occupancy of the periplasmic $\mathrm{Cu_B}$ site. Electron paramagnetic resonance (EPR) spectroscopic data indicate that the $\mathrm{Cu_B}$ site is primarily occupied by Cu(II), while $\mathrm{Cu_C}$ and $\mathrm{Cu_D}$ are primarily occupied by diamagnetic ions, presumably Cu(I). Notably, a lipid molecule is bound between the $\mathrm{Cu_C}$ and $\mathrm{Cu_D}$ sites, separating them by ∼8.0 Å. The results underscore the importance of studying these enzymes in their native environments across species to resolve conserved and divergent molecular features.

Introduction

Methane- and ammonia-oxidizing bacteria consume methane and release nitrous oxide, respectively, regulating atmospheric levels of these potent greenhouse gases.[1] In the first steps of their metabolic pathways, methane oxidizers convert methane to methanol while ammonia oxidizers convert ammonia to hydroxylamine.[2,3] These challenging chemical reactions are catalyzed by homologous copper-dependent, membrane-bound enzymes: particulate methane monooxygenase (pMMO) and ammonia monooxygenase (AMO).[4–6] Understanding the molecular chemistry of these enzymes is of substantial interest for both environmental and biotechnological applications.[7–10]

Initial crystal structures of pMMO, derived from inactive, detergent-solubilized samples, revealed an ∼300 kDa complex comprising three copies each of the PmoA, PmoB, and PmoC subunits.[11] These structures also revealed three mononuclear copper-binding sites—the bis-His, $\mathrm{Cu_B}$, and $\mathrm{Cu_C}$ sites.[5] However, the crystal structures lacked parts of PmoA and PmoC, including a highly conserved portion of PmoC adjacent to $\mathrm{Cu_C}$ in the transmembrane region.[12] This region was later resolved by reconstituting pMMO into lipid nanodiscs, discoidal lipid bilayers that partially restore pMMO activity, especially when prepared with native lipids extracted from whole cells of methane-oxidizing bacteria.[13] High resolution cryoEM structures of these nanodisc samples revealed the missing portions of PmoA and PmoC, stabilized by interacting lipids, along with a previously unknown copper-binding site denoted $\mathrm{Cu_D}$, located within 6 Å of $\mathrm{Cu_C}$. Combined cryoEM and spectroscopic data then showed that a hydrophobic pocket adjacent to $\mathrm{Cu_D}$ binds the product analog trifluoroethanol, pinpointing this region as the likely active site.[14]

In multiple structures of active *Methylococcus capsulatus* (Bath) pMMO in lipid nanodiscs, $\mathrm{Cu_D}$ is occupied while $\mathrm{Cu_C}$ is empty. By contrast, structures of inactive *Methylotuvimicrobium alcaliphilum* 20Z and *Methylocystis* sp. Rockwell pMMOs in lipid nanodiscs contained occupied $\mathrm{Cu_C}$ sites with disordered $\mathrm{Cu_D}$ sites.[13] These observations raised significant questions regarding the relationship between $\mathrm{Cu_C}$ and $\mathrm{Cu_D}$, the possibility of simultaneous occupancy, and the role of lipids in pMMO function. In addition, the potential effects of purification and nanodisc reconstitution on the pMMO structure and copper sites remained unclear. To avoid structural distortions caused

---

[a] *Departments of Molecular Biosciences and of Chemistry, Northwestern University, Evanston, Illinois 60208, USA*

[b] *Department of Biological Sciences, University of Alberta, Edmonton, AB, Canada T6G 2E9. E-mail: amyr@northwestern.edu*

by purification, cryoEM single particle analysis (SPA) was then used to obtain structures of *M. capsulatus* (Bath) and *M.* sp. Rockwell pMMOs directly in native membranes.[15] In both structures, Cu_D is occupied and Cu_C is vacant. Thus, Cu_D is present in pMMO from multiple species, supporting its identification as the active site.[14]

Attempts to characterize AMO had been hindered by its instability outside the membrane and the slow growth rates of ammonia-oxidizing bacteria, which precluded obtaining sufficient cell mass for structural studies.[6,16] Recently, however, cryoEM SPA of native membranes also enabled structure determination of AMO from *Nitrosomonas europaea* (ATCC 19718).[15] Like pMMO, *N. europaea* AMO is an $\alpha_3\beta_3\gamma_3$ trimer formed by the AmoA, AmoB, and AmoC subunits and contains Cu_B, Cu_C, and Cu_D binding sites. Notably, the *N. europaea* AMO structure revealed a previously unknown supernumerary helical subunit interacting with AmoC. In contrast to the native membrane pMMO structures, Cu_C is occupied while Cu_D is empty in the *N. europaea* AMO structure, deepening the mystery of these neighboring copper sites and underscoring the need for more data to establish a structural catalog of potential active-site copper occupancies and conformations.

Here we determined the 2.6 Å resolution cryoEM structure of AMO from *Nitrosospira briensis* C-128 (ref. 17) in native membranes, and assessed the Cu(II) occupancy of the metal-binding sites by electron paramagnetic resonance (EPR) spectroscopy. Surprisingly, the structure reveals a new active-site conformation with both Cu_C and Cu_D occupied, apparently with a phospholipid molecule wedged between them. This arrangement represents a dramatic deviation from those observed in prior AMO and pMMO structures, despite all being derived from native membranes with minimal biochemical manipulation. As such, it opens the possibility of catalytic involvement of both copper sites, which here are presumably occupied with Cu(I), and conceivably of lipids in the pMMO and AMO reactions. Further, this structure highlights the importance of studying pMMOs and AMOs across species to develop a comprehensive model of their molecular features.

Results and discussion

Membranes were isolated from ~0.5 g of *N. briensis* cells. While both betaproteobacteria, *N. europaea* and *N. briensis* belong to divergent phyla,[18] with 78, 85, and 88% identity of the AmoB, AmoA, and AmoC subunits, respectively. In addition, the two species have different intracytoplasmic membrane morphologies.[19] The *N. briensis* membranes were applied to grids for data collection and SPA (Fig. S1). Like *N. europaea* AMO and the previously studied pMMOs,[15,20] *N. briensis* AMO forms hexagonal arrays in the membranes (Fig. 1A). The 2.6 Å resolution structure reveals a trimer, similar to prior pMMO and AMO structures, with numerous bound lipids encasing the transmembrane region (Fig. 1B and C). There is no density corresponding to supernumerary helices like those identified in *N.*

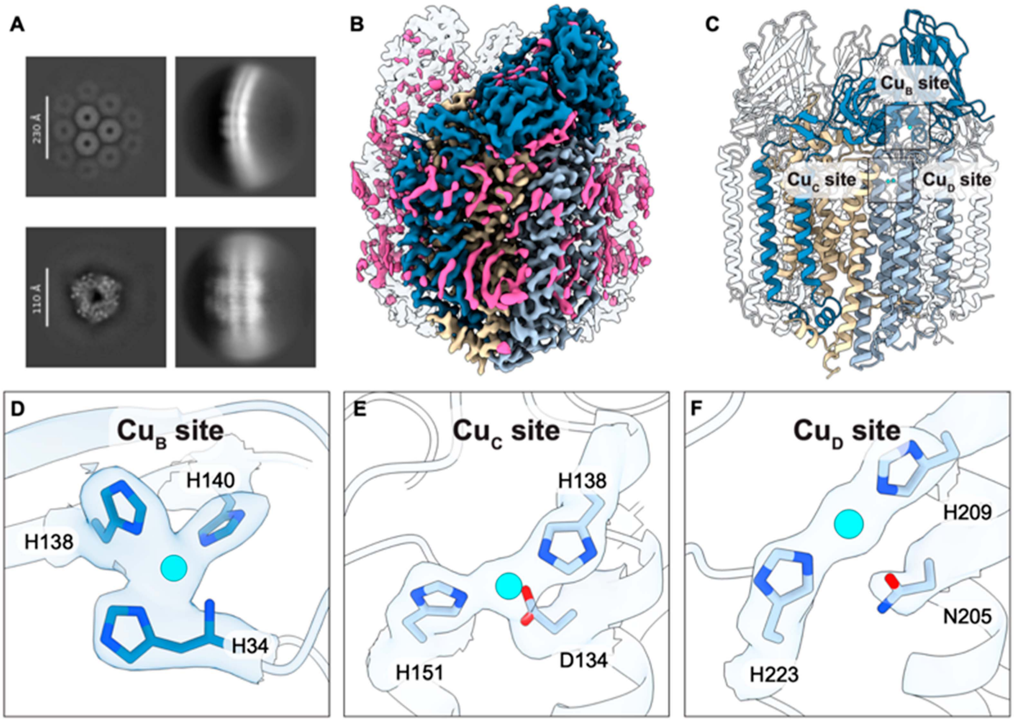

Fig. 1 Structure of *N. briensis* AMO in native membranes. (A) 2D class averages showing secondary structure features, the membrane, and hexagonal arrays from (left) top-down and (right) side-on views at box sizes of 640 (top) and 320 (bottom) pixels. (B) 2.6 Å resolution cryoEM map with one protomer highlighted showing AmoB (blue), AmoA (wheat), AmoC (light blue), and membrane-associated densities (pink). (C) Ribbon model with same coloring as (B). (D) Cu_B site with density superimposed (5σ). (E) Cu_C site with density superimposed (5σ). (F) Cu_D site with density superimposed (5σ).

europaea AMO (Fig. S2),[15] suggesting that such subunits are not present in, or at least not strongly associated with, all AMOs.

Inspection of the cryoEM map revealed three occupied metal-binding sites. First, the Cu_B site is occupied and exhibits the same coordination as observed in all pMMO structures[5] and in the *N. europaea* AMO structure:[15] three nitrogen atoms from histidine side chains and the amino terminal nitrogen of AmoB (Fig. 1D). The PmoB bis-His site[5] is not present in AMOs, as one of the histidine ligands is replaced by glutamine. Second, the Cu_C site is clearly occupied by a metal ion coordinated by two histidines (His138, His151) and an aspartate residue (Asp134), consistent with previous pMMO and AMO structures.[13,15] Surprisingly, the Cu_D site is also occupied, providing the first evidence for simultaneous occupancy of Cu_C and Cu_D as well as for the presence of Cu_D in AMO. The metal ion in the Cu_D site is coordinated by two histidine residues (His209, His223) in a linear, two-coordinate geometry (Fig. 1F). The side chain oxygen of the asparagine residue (Asn205) that typically coordinates Cu_D in pMMOs is >3 Å from the copper ion.

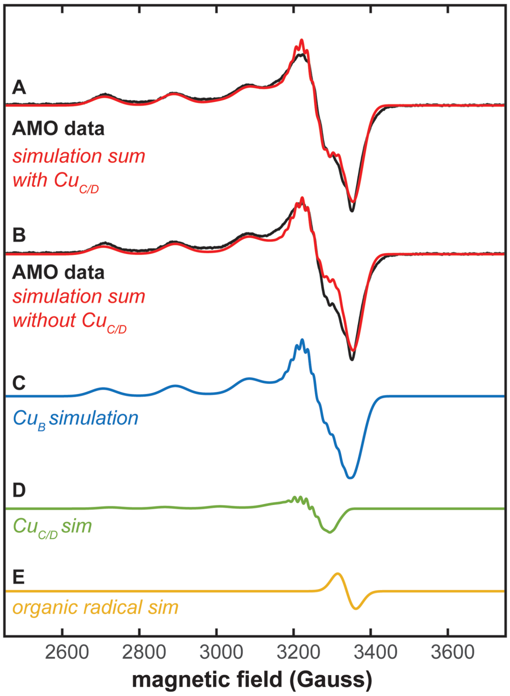

Fig. 2 EPR spectroscopy of *N. briensis* AMO in native membranes. (A) EPR spectrum of *N. briensis* AMO in native membranes overlaid with a simulation that includes contributions from Cu_B, $Cu_{C/D}$, and an organic free radical with $g \sim 2$. In this simulation, Cu_B comprises 87% of the total Cu(II) and $Cu_{C/D}$ makes up 13% of the total Cu(II). (B) EPR spectrum of *N. briensis* AMO in native membranes overlaid with a simulation that includes only the contributions from Cu_B and the organic free radical. (C) The Cu_B component of the simulations in (A and B). (D) The Cu_C/Cu_D component of the simulation in (A). (E) The organic free radical component of simulations in (A and B). EPR conditions: 9.376 GHz microwave frequency, 200 μW microwave power, temperature 20 K, 320 ms time constant, 12.5 G modulation, 20 scans, 100 s per scan. EPR simulation parameters: **g**-tensors and hyperfine couplings adapted from ref. 21, Cu_B $\mathbf{g} = [2.243, 2.068, 2.035]$, $\mathbf{A}(^{63/65}Cu) = [572, 15, 14]$ MHz, $\mathbf{A}(^{14}N_a) = [34.2, 38.5, 38.5]$ MHz, $\mathbf{A}(^{14}N_b) = [37.8, 38.5, 38.5]$ MHz, $\mathbf{A}(^{14}N_c) = [37.8, 38.5, 38.5]$ MHz, $\mathbf{A}(^{14}N_d) = [37.8, 47.0, 47.0]$ MHz. $Cu_{C/D}$ $\mathbf{g} = [2.28, 2.07, 2.05]$, $\mathbf{A}(^{63/65}Cu) = [440, 40, 20]$ MHz, $\mathbf{A}(^{14}N_a) = [34.2, 38.5, 38.5]$ MHz, $\mathbf{A}(^{14}N_b) = [37.8, 47.0, 47.0]$. The organic free radical was simulated as $g = 2.0$ with $H_{strain} = [60, 60, 60]$ MHz. Copper hyperfine couplings were simulated with natural abundance mixtures of ^{63}Cu and ^{65}Cu. The respective weights used in the summed simulation are 13% $Cu_{C/D}$ and 87% Cu_B.

The occupancy of Cu(II) in these three sites was assessed by EPR spectroscopy of the same sample of *N. briensis* membranes used for cryoEM (Fig. 2A). Given that the coordination spheres of the three metal binding sites identified by cryoEM are essentially identical to those in pMMO, we assume that the spectra from a Cu(II) ion in each site should be characterized by the spin Hamiltonian parameters obtained previously for those sites in pMMO, with essentially identical parameters for Cu_C and Cu_D ($\mathbf{g} = [2.29, 2.07, 2.05]$ and ^{63}Cu $A_{\parallel} = 575$ MHz), distinct from those for Cu_B ($\mathbf{g} = [2.241, 2.068, 2.035]$ and ^{63}Cu $A_{\parallel} = 575$ MHz).[21,22] The Cu hyperfine coupling in the $g_{\parallel}$ region of the AMO spectrum is incompatible with a simulation that assumes the spectrum arises from the Cu_C/Cu_D sites (Fig. S3). Instead, the spectrum agrees with that of Cu_B, in particular matching well in the $g_{\parallel}$ region. The simulated spectrum in the $g_{\perp}$ region is improved by inclusion of a small contribution from a free-radical with $g \sim 2$ (Fig. 2A, B and E). In addition, this region is further improved by assuming the AMO spectrum includes a minority contribution from the Cu_C/Cu_D sites (Fig. 2A), which together account for roughly ∼13% of the total Cu(II) signal (Fig. 2C and D).

These data suggest that the Cu_C/Cu_D sites are primarily occupied by EPR-silent Cu(I). The dominance of the AMO signal by Cu_B(II) is analogous to what is observed for pMMO,[5,22] in which the Cu_C/Cu_D sites are present as Cu(I) *in vivo* and remain mostly reduced in native membranes, with oxidation occurring only upon solubilization in detergent and enzyme purification.[21,22] Air oxidation of the AMO-containing sample did not lead to a significantly more intense Cu_C/Cu_D signal (Fig. S4), even upon bubbling with O_2, suggesting that these membrane-bound sites may be more resistant to oxidation than the Cu_C/Cu_D sites in pMMO, or may be occupied in some part by non-copper, EPR-silent ions such as Zn(II). Since methane is also a substrate for AMOs,[23] the sample was tested for methane oxidation activity using an established assay,[24] but no methanol was detected. The absence of activity could be related to the difficulty oxidizing the Cu_C/Cu_D sites.

While both Cu_C and Cu_D are occupied by metal ions, presumably Cu(I) based on the EPR spectra and those of previous samples of pMMO and AMO, the two sites are significantly farther apart than predicted by previous pMMO and AMO cryoEM structures (Fig. 3A–D).[13,15] In the previous structures, when either Cu_C or Cu_D is occupied, the ligands for the other site are oriented such that a second copper ion would be located ∼4.5–5.6 Å away (Fig. 3E, F and S5). By contrast, the two copper ions modeled in *N. briensis* AMO are separated by ∼8.0 Å (Fig. 3C). The active-site pocket is filled with a nonprotein density that appears to wedge the two copper sites apart (Fig. 3A–D). This density resembles a two-tailed phospholipid, showing clear densities for a headgroup and two acyl chains that extend into the transmembrane region, flanked by the three conserved phenylalanine residues that line the active site

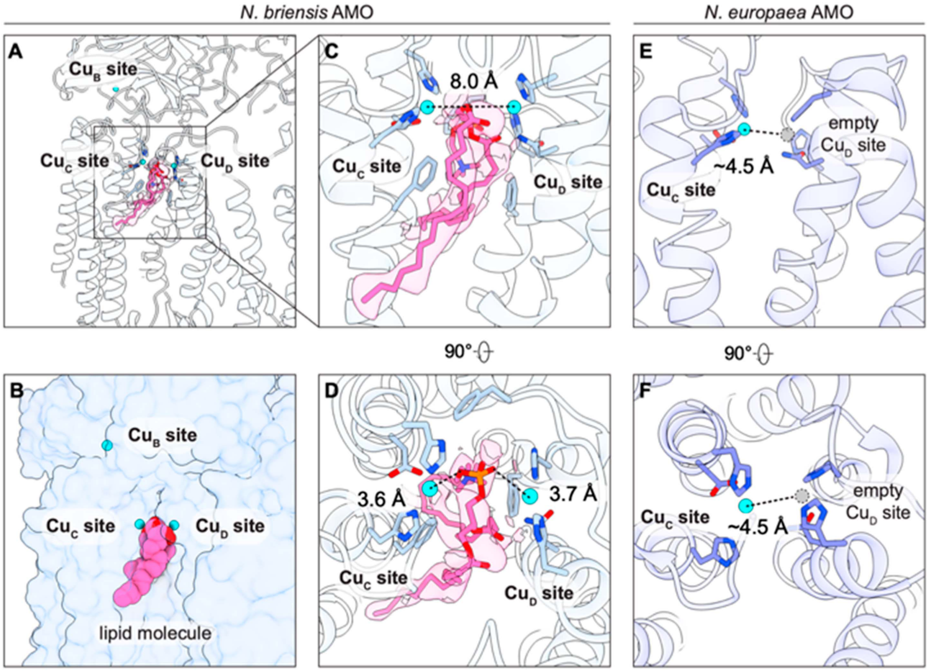

Fig. 3 Simultaneous occupancy of Cu_C and Cu_D in *N. briensis* AMO in native membranes. (A) Side-on view showing the locations of the Cu_B, Cu_C, and Cu_D sites. (B) Transparent surface representation of *N. briensis* AMO with the lipid wedged in its active site, shown using a space-filling representation. Although the lipid is lodged between the Cu_C and Cu_D sites, it is not completely buried and appears to be accessible to the membrane, providing a possible route for its entry into the active site. (C) Zoomed-in view of (A) showing the Cu_C and Cu_D sites with a lipid molecule (modeled as POPC) wedged in the active-site pocket. The cryoEM density is superimposed on the Cu_C and Cu_D sites (5σ) and the modeled POPC lipid (3σ). (D) Top-down view of the Cu_C and Cu_D sites showing their approximate distances from the nearest oxygen atoms of the modeled POPC molecule. (E) Side-on view of the *N. europaea* AMO active site with an occupied Cu_C site and an empty Cu_D site. The location of a modeled copper ion in the Cu_D site is shown as a gray circle. (F) Top-down view of (E).

as identified by trifluoroethanol binding to pMMO (Fig. 3C and D).[14] The density is well modeled as 1-palmitoyl-2-oleoyl-*sn*-glycero-3-phosphocholine (POPC) (Fig. 3A–C). A lipid of this chain length is consistent with reported lipid compositions for ammonia oxidizers.[25,26] The lipid does not appear to coordinate the copper centers, with the oxygen atoms of its phosphate group ~3.6–3.7 Å from both Cu_C and Cu_D (Fig. 3C).

The presence of this lipid shifts the helix containing Cu_D ligands Asn205 and His209 markedly from its position in the *N. europaea* AMO structure (Fig. 4). This conformational change is

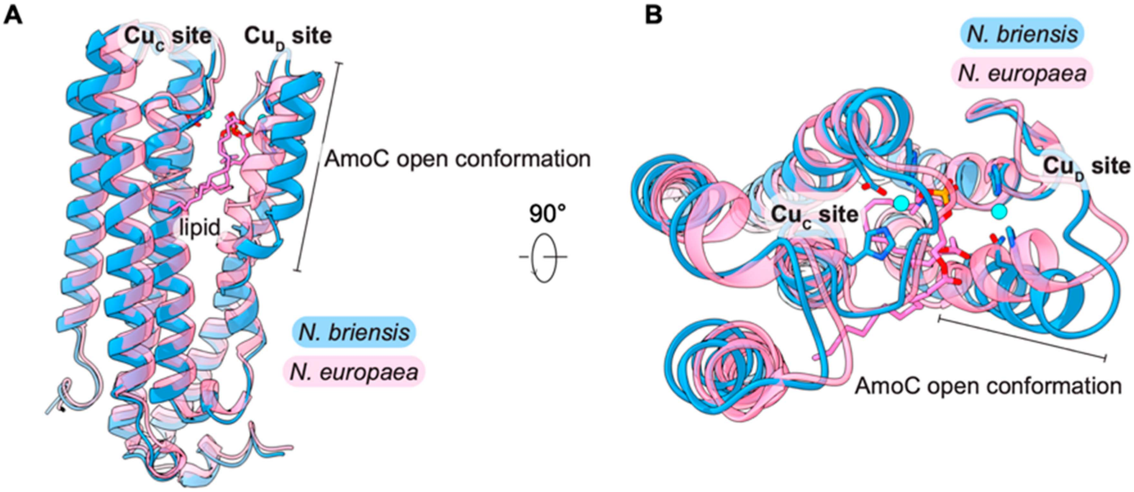

Fig. 4 Superposition of the AmoC subunits from the *N. europaea* (pink) and *N. briensis* (blue) AMO structures in native membranes shown as side-on (A) and top–down (B) views. Ligands to the Cu_C and Cu_D sites in *N. briensis* AMO are shown as sticks and copper ions are shown as cyan spheres. Only the Cu_C site is occupied in the *N. europaea* AMO structure.

facilitated by the presence of a conserved proline residue (Pro200)[12] that introduces a kink in the helix, bending it toward the central opening of the AMO trimer (Fig. S6). The resultant open conformation of AmoC (spanning residues 194–217) is accommodated by a shift in residues 205–215 of the AmoA subunit. While this region of AmoC and PmoC is clearly flexible, as evidenced by its disorder in pMMO crystal structures,[12] this conformation has not been observed previously. The lipid itself is partially exposed in the groove between protomers, suggesting it originates from this region (Fig. 3B).

Conclusions

The discovery of the pMMO Cu_D center[13] raised critical questions regarding the active site, with the looming possibility that it could be dinuclear. Until now, simultaneous occupancy of Cu_C and Cu_D had not been observed, even computationally,[27] precluding substantiated consideration of such a model. The present *N. briensis* AMO structure clearly shows density attributable to copper in both sites with an ~8 Å separation imposed by an intervening lipid molecule. Importantly, the structure was determined directly from native membranes without biochemical manipulation. Thus, this lipid represents the first example of an endogenous molecule bound in the pMMO/AMO active site and could be relevant to function. Attempts to load the two sites *in vitro* with Cu(II), Cu(I), a mixture thereof, or other metal ions have not been successful, suggesting a potential scenario in which increased spatial separation facilitates dual copper loading *in vivo*. The structure may represent a loading conformation, in which Cu_C exists as a copper repository for a mononuclear Cu_D catalytic center.

Alternatively, the two sites may both be occupied during catalysis, perhaps moving closer together, either to the predicted 4.5–5.6 Å separation or even closer, although there is no spectroscopic evidence for a coupled dicopper cluster. In general, occupancy of Cu_D correlates with activity, with Cu_D occupied and Cu_C empty in structures of active *M. capsulatus* (Bath) pMMO in lipid nanodiscs[13] and native membranes[15] as well as structures with the product analog and inhibitor trifluoroethanol.[14] By contrast, only Cu_C is occupied in structures of inactive *M. alcaliphilum* 20Z and *M.* sp. Rockwell pMMOs in lipid nanodiscs[13] as well as in all pMMO crystal structures, in which the Cu_D site and surrounding residues are not observed.[12] However, only Cu_D is occupied in the structure of inactive *M.* sp. Rockwell pMMO in native membranes.[15] In the case of AMO, Cu_C is occupied in *N. europaea* AMO, and both sites are occupied in the current *N. briensis* pMMO structure; neither AMO exhibited activity, but sample limitations precluded extensive activity studies. However, it remains possible that the copper centers in different pMMO and AMO membrane samples are differentially disrupted upon cryoEM grid preparation. Given these considerations, it is difficult to correlate structure with activity.

One possibility is that both Cu_C and Cu_D are involved in activity, but are more conformationally flexible that typical dicopper centers.[28] Notably, recent studies of the dicopper enzymes dopamine β-hydroxylase and peptidylglycine monooxygenase suggest a more dynamic picture than envisioned previously, with Cu–Cu distances spanning 4–14 Å.[29–33] Further, several new classes of enzymes containing two copper-binding sites have emerged recently, including the BURP-domain peptide cyclases[34] and copper-dependent halogenases.[35] In the BURP-domain cyclases, two binding sites each with two histidine ligands are predicted to be separated by 7 Å,[34] and may also adopt multiple conformations.[36] Whether pMMO and AMO exhibit similar dynamics, perhaps mediated by lipids, remains to be established.

Materials and methods

Culturing of *Nitrosospira briensis* C-128

N. briensis C-128 was cultured in 1 L Wheaton bottles sealed with inlayed rubber butyl caps. HEPES-buffered HK medium (200 mL) containing 10 mM $(NH_4)_2SO_4$ and 0.5% (v/v) phenol red was inoculated with 2% v/v late log phase culture.[37] Cultures were incubated at 28 °C in the dark with shaking at 150 rpm and the pH was adjusted daily as needed with 5% (w/v) Na_2CO_3 to maintain pH 7.5–8.0. Growth was measured by NO_2^- production.[38] To harvest biomass, cultures that achieved *ca.* 90% NH_3 conversion to NO_2^- were centrifuged at 5000 × *g* for 45 min. Cell pellets were transferred to 15 mL sterile Falcon tubes and centrifuged at 2000 × *g* for 15 min to completely remove supernatant. Pellets were flash-frozen in a −70 °C ethanol bath and shipped on dry ice.

Isolation of *N. briensis* membranes

Approximately 0.5 g of *N. briensis* cells were resuspended in buffer containing 25 mM PIPES (pH 7.3) and 250 mM NaCl with DNase (Sigma-Aldrich) and EDTA-free complete protease inhibitor cocktail (Sigma-Aldrich). The resuspended cells were lysed at 4 °C by sonication at 80% power (45 amplitude, 1 second on and 1 second off) for 10 min using a QSonica Q700 instrument. The lysate was clarified by centrifugation at 10 000 × *g* for 45 min. The supernatant was preserved, and membranes were isolated from this supernatant by ultracentrifugation at 150 000 × *g* for 1 h. The pellet was then harvested and resuspended in 200 μL of lysis buffer with a Dounce homogenizer.

CryoEM grid preparation and screening

Isolated membranes from *N. briensis* were diluted to 4 mg mL^{-1} of total protein as measured by the DC Lowry (Bio-Rad) assay. This sample was then blotted and plunge frozen in liquid ethane on C-Flat holey carbon copper grids with 1.2 μm holes, 1.3 μm spacing, and 400 mesh (Electron Microscopy Sciences) with an FEI Vitrobot. Prior to blotting, grids were plasma cleaned using a Solarus plasma cleaner (Gatan) for 10 s at a voltage of 10 W. 3 μL of sample were applied to the grids in the Vitrobot chamber set to 100% humidity and 4 °C and blotted for 4 s with a blot force of 5 and a wait time of 30 s followed by vitrification in liquid ethane.

CryoEM data collection

Grids were screened in the Structural Biology Facility at Northwestern using a 200 kV Glacios (Thermo-Fisher) microscope. Suitable grids were identified for high resolution data collection at the National Center for CryoEM Access and Training (NCCAT) using a Titan Krios microscope (Thermo-Fisher) operating at 300 kV and controlled by Leginon. Details regarding the data collection parameters are provided in Table S1.

CryoEM data processing and analysis

CryoEM data were processed using cryoSPARC v4.[39] Movie frames were aligned using patch motion correction, and contrast transfer function (CTF) parameters were estimated using patch CTF estimation.[40] Particle picking was performed first using template picking with the map of *N. europaea* AMO in native membranes, EMD-45663, as a preliminary template. Particles were curated extensively using 2D classification and heterogenous refinement to obtain clear top-down and side-on views of AMO, which were used to train a Topaz picking model.[41,42] Topaz picking was then used to generate a stack of particles which were curated using multiple rounds of heterogenous refinement, using EMD-45663 as a reference volume with EMD-45663 lowpass filtered to 100 Å resolution as a decoy volume. These particles were then refined using non-uniform refinement[43] at C_1 and then C_3 symmetry. Global and local CTF refinements were alternated with non-uniform refinements to improve map resolution and quality, followed by local motion correction and a final round of non-uniform refinement. Finally, local resolution estimation and local sharpening was used to sharpen the final volume. Resolution is reported based on gold-standard Fourier shell correlation with a cutoff of 0.143.[44]

Model building, refinement, and visualization

An initial structural model was built into the final cryoEM map using ModelAngelo.[45] Copper ions and lipids were manually added to the structure, inspected, and adjusted using Coot [version 0.9.8.93 EL (ccp4)].[46] Further refinement of this model was performed using real-space refinement using the Phenix (version 1.21-5207)[47] cryoEM suite along with automatic addition of waters, followed by manual inspection using Coot. Refined models were fitted into cryoEM maps, structures were visualized, maps were resampled to a uniform grid spacing, contour thresholds were chosen using sigma (σ) values, and figures were generated using ChimeraX-1.7.1.[47]

EPR spectroscopy

CW (continuous wave) X-band EPR measurements were performed on a Bruker ESP-300 spectrometer with an Oxford Instruments ESR-900 liquid helium flow cryostat. All spectra were background subtracted. Samples were prepared at ~25 mg mL^{-1} protein (~250 μM AMO protomer) in 25 mM PIPES (pH 7.3) containing 250 mM NaCl. EPR samples were prepared in parallel to cryoEM samples and loaded into custom quartz EPR tubes, flash frozen in liquid nitrogen, and stored in a liquid nitrogen dewar until analysis. EPR simulations were performed using EasySpin.[48]

Methane oxidation activity assay

AMO membrane preparations (100 μL) were diluted to 0.5–2 mg mL^{-1} total protein and combined with 4 mg per mL NADH in 2 mL screw-cap vials (Agilent). After sealing, 1 mL of headspace was withdrawn and replaced with 1.5 mL of ^{13}C-methane (Sigma-Aldrich). Three technical replicates were prepared for each independent sample, and control vials lacking methane and NADH were included. Reactions were shaken at 200 rpm in a 30 °C water bath for 5 min, then quenched by freezing at −20 °C. GC/MS analysis of ^{13}C-methanol production was performed exactly as described previously.[15]

Author contributions

F. J. T. and A. C. R. designed experiments, F. J. T. performed structural and biochemical analysis; F. J. T. and A. C. R. analyzed structural data; A. A. B. T. and L. Y. S. cultured *N. briensis* C-128; B. M. H. and M. B. H. performed EPR analysis; F. J. T. and A. C. R. wrote the paper with input from M. B. H., L. Y. S., and B. M. H.

Conflicts of interest

The authors declare no competing financial interest.

Data availability

The model and corresponding cryoEM map of *N. briensis* C-128 AMO have been deposited in the Protein Data Bank and Electron Microscopy Data Bank with accession codes PDB 9PXF and EMDB EMD-71966.

Supplementary information (SI): Table S1 and Fig. S1–S6. See DOI: https://doi.org/10.1039/d5sc08447d.

Acknowledgements

This work was supported by Department of Energy grants DE-SC0016284 (A. C. R.) and DE-SC0019342 (B. M. H.), and NIH grants R35GM118035 (A. C. R.) and R01GM111097 (B. M. H.). L. Y. S. and A. A. B. T. were supported by NSERC-DG grant RGPIN-2025-04834. F. J. T. was supported by NIH grant F31ES034283. Some of this work was performed at the National Center for CryoEM Access and Training (NCCAT) and the Simons Electron Microscopy Center located at the New York Structural Biology Center, supported by the NIH Common Fund Transformative High-Resolution Cryo-Electron Microscopy program (U24 GM129539) and by Grants from the Simons Foundation (SF349247) and NY State Assembly.

References

1 L. Y. Stein and M. E. Lidstrom, Greenhouse gas mitigation requires caution, *Science*, 2024, **384**, 1068–1069.

2 R. S. Hanson and T. E. Hanson, Methanotrophic bacteria, *Microbiol. Rev.*, 1996, **60**, 439–471.

3 D. J. Arp and L. Y. Stein, Metabolism of inorganic N compounds by ammonia-oxidizing bacteria, *Crit. Rev. Biochem. Mol. Biol.*, 2003, **38**, 471–495.

4 A. J. Holmes, A. Costello, M. E. Lidstrom and J. C. Murrell, Evidence that particulate methane monooxygenase and ammonia monooxygenase may be evolutionarily related, *FEMS Microbiol. Lett.*, 1995, **132**, 203–208.

5 F. J. Tucci and A. C. Rosenzweig, Direct methane oxidation by copper- and iron-dependent methane monooxygenases, *Chem. Rev.*, 2024, **124**, 1288–1320.

6 K. M. Lancaster, J. D. Caranto, S. H. Majer and M. A. Smith, Alternative bioenergy: updates to and challenges in nitrification metalloenzymology, *Joule*, 2018, **2**, 421–441.

7 N. K. Kang, T. H. T. Chau and E. Y. Lee, Engineered methane biocatalysis: strategies to assimilate methane for chemical production, *Curr. Opin. Biotechnol.*, 2024, **85**, 103031.

8 D. Sauvageau, L. Y. Stein, E. Arenas, S. Das, M. Iacobelli, M. Lawley, M. Lazic, F. L. Rondón and C. Weiblen, Industrializing methanotrophs and other methylotrophic bacteria: from bioengineering to product recovery, *Curr. Opin. Biotechnol.*, 2024, **88**, 103167.

9 S. Wendeborn, The chemistry, biology, and modulation of ammonium nitrification in soil, *Angew. Chem., Int. Ed. Engl.*, 2020, **59**, 2182–2202.

10 X. Wang, J. Bai, T. Xie, W. Wang, G. Zhang, S. Yin and D. Wang, Effects of biological nitrification inhibitors on nitrogen use efficiency and greenhouse gas emissions in agricultural soils: a review, *Ecotoxicol. Environ. Saf.*, 2021, **220**, 112338.

11 R. L. Lieberman and A. C. Rosenzweig, Crystal structure of a membrane-bound metalloenzyme that catalyses the biological oxidation of methane, *Nature*, 2005, **434**, 177–182.

12 C. W. Koo and A. C. Rosenzweig, Biochemistry of aerobic biological methane oxidation, *Chem. Soc. Rev.*, 2021, **50**, 3424–3436.

13 C. W. Koo, F. J. Tucci, Y. He and A. C. Rosenzweig, Recovery of particulate methane monooxygenase activity in a lipid bilayer, *Science*, 2022, **375**, 1287–1291.

14 F. J. Tucci, R. J. Jodts, B. M. Hoffman and A. C. Rosenzweig, Product analog binding identifies the copper active site of particulate methane monooxygenase, *Nat. Catal.*, 2023, **6**, 1194–1204.

15 F. J. Tucci and A. C. Rosenzweig, Structures of methane and ammonia monooxygenases in native membranes, *Proc. Natl. Acad. Sci. U. S. A.*, 2025, **122**, e2417993121.

16 L. Y. Stein, Insights into the physiology of ammonia-oxidizing microorganisms, *Curr. Opin. Chem. Biol.*, 2019, **49**, 9–15.

17 M. C. Rice, J. M. Norton, F. Valois, A. Bollmann, P. J. Bottomley, M. G. Klotz, H. J. Laanbroek, Y. Suwa, L. Y. Stein, L. Sayavedra-Soto, T. Woyke, N. Shapiro, L. A. Goodwin, M. Huntemann, A. Clum, M. Pillay, N. Kyrpides, N. Varghese, N. Mikhailova, V. Markowitz, K. Palaniappan, N. Ivanova, D. Stamatis, T. B. K. Reddy, C. Y. Ngan and C. Daum, Complete genome of *Nitrosospira briensis* C-128, an ammonia-oxidizing bacterium from agricultural soil, *Stand. Genomic Sci.*, 2016, **11**, 46.

18 U. Purkhold, M. Wagner, G. Timmermann, A. Pommerening-Röser and H. P. Koops, 16S rRNA and *amoA*-based phylogeny of 12 novel betaproteobacterial ammonia-oxidizing isolates: extension of the dataset and proposal of a new lineage within the nitrosomonads, *Int. J. Syst. Evol. Microbiol.*, 2003, **53**, 1485–1494.

19 H.-P. Koops, U. Purkhold, A. Pommerening-Röser, G. Timmermann and M. Wagner, in *The Prokaryotes: Volume 5: Proteobacteria: Alpha and Beta Subclasses*, ed. M. Dworkin, S. Falkow, E. Rosenberg, K.-H. Schleifer and E. Stackebrandt, Springer, New York, NY, 2006, pp. 778–811.

20 Y. A. Zhu, C. W. Koo, C. K. Cassidy, M. C. Spink, T. Ni, L. C. Zanetti-Domingues, B. Bateman, M. L. Martin-Fernandez, J. Shen, Y. W. Sheng, Y. Song, Z. Y. Yang, A. C. Rosenzweig and P. J. Zhang, Structure and activity of particulate methane monooxygenase arrays in methanotrophs, *Nat. Commun.*, 2022, **13**, 5221.

21 M. O. Ross, F. MacMillan, J. Wang, A. Nisthal, T. J. Lawton, B. D. Olafson, S. L. Mayo, A. C. Rosenzweig and B. M. Hoffman, Particulate methane monooxygenase contains only mononuclear copper centers, *Science*, 2019, **364**, 566–570.

22 R. J. Jodts, M. O. Ross, C. W. Koo, P. E. Doan, A. C. Rosenzweig and B. M. Hoffman, Coordination of the copper centers in particulate methane monooxygenase: comparison between methanotrophs and characterization of the $\mathrm{Cu_c}$ site by EPR and ENDOR spectroscopies, *J. Am. Chem. Soc.*, 2021, **143**, 15358–15368.

23 M. R. Hyman and P. M. Wood, Methane oxidation by *Nitrosomonas europaea*, *Biochem. J.*, 1983, **212**, 31–37.

24 S. Y. Ro, M. O. Ross, Y. W. Deng, S. Batelu, T. J. Lawton, J. D. Hurley, T. L. Stemmler, B. M. Hoffman and A. C. Rosenzweig, From micelles to bicelles: Effect of the membrane on particulate methane monooxygenase activity, *J. Biol. Chem.*, 2018, **293**, 10457–10465.

25 M. Blumer, T. Chase and S. W. Watson, Fatty acids in the lipids of marine and terrestrial nitrifying bacteria, *J. Bacteriol.*, 1969, **99**, 366–370.

26 M. Kruse, S. Keuter, E. Bakker, E. Spieck, T. Eggers and A. Lipski, Relevance and diversity of Nitrospira populations in biofilters of brackish RAS, *PLoS One*, 2013, **8**, e64737.

27 W. Peng, Z. Wang, Q. Zhang, S. Yan and B. Wang, Unraveling the valence state and reactivity of copper centers in membrane-bound particulate methane monooxygenase, *J. Am. Chem. Soc.*, 2023, **145**, 25304–25317.

28 I. Kipouros and E. I. Solomon, New mechanistic insights into coupled binuclear copper monooxygenases from the recent elucidation of the ternary intermediate of tyrosinase, *FEBS Lett.*, 2023, **597**, 65–78.

29 S. Maheshwari, C. Shimokawa, K. Rudzka, C. D. Kline, B. A. Eipper, R. E. Mains, S. B. Gabelli, N. Blackburn and L. M. Amzel, Effects of copper occupancy on the conformational landscape of peptidylglycine α-hydroxylating monooxygenase, *Commun. Biol.*, 2018, **1**, 74.

30 T. V. Vendelboe, P. Harris, Y. Zhao, T. S. Walter, K. Harlos, K. El Omari and H. E. Christensen, The crystal structure of human dopamine β-hydroxylase at 2.9 Å resolution, *Sci. Adv.*, 2016, **2**, e1500980.

31 E. F. Welch, K. W. Rush, R. J. Arias and N. J. Blackburn, Copper monooxygenase reactivity: Do consensus mechanisms accurately reflect experimental observations?, *J. Inorg. Biochem.*, 2022, **231**, 111780.

32 R. J. Arias, E. F. Welch and N. J. Blackburn, New structures reveal flexible dynamics between the subdomains of peptidylglycine monooxygenase. Implications for an open to closed mechanism, *Protein Sci.*, 2023, **32**, e4615.

33 E. F. Welch, K. W. Rush, K. A. S. Eastman, V. Bandarian and N. J. Blackburn, The binuclear copper state of peptidylglycine monooxygenase visualized through a selenium-substituted peptidyl-homocysteine complex, *Dalton Trans.*, 2025, **54**, 4941–4955.

34 L. S. Mydy, J. Hungerford, D. N. Chigumba, J. R. Konwerski, S. C. Jantzi, D. Wang, J. L. Smith and R. D. Kersten, An intramolecular macrocyclase in plant ribosomal peptide biosynthesis, *Nat. Chem. Biol.*, 2024, **20**, 530–540.

35 C. Y. Chiang, M. Ohashi, J. Le, P. P. Chen, Q. Zhou, S. Qu, U. Bat-Erdene, S. Hematian, J. A. Rodriguez, K. N. Houk, Y. Guo, J. A. Loo and Y. Tang, Copper-dependent halogenase catalyses unactivated C–H bond functionalization, *Nature*, 2025, **638**, 126–132.

36 N. J. Blackburn, Metal-mediated peptide processing. How copper and iron catalyze diverse peptide modifications such as amidation and crosslinking, *RSC Chem. Biol.*, 2025, **6**, 1048–1067.

37 A. Krümmel and H. Harms, Effect of organic matter on growth and cell yield of ammonia-oxidizing bacteria, *Arch. Microbiol.*, 1982, **133**, 50–54.

38 A. Bollmann, E. French and H. J. Laanbroek, Isolation, cultivation, and characterization of ammonia-oxidizing bacteria and archaea adapted to low ammonium concentrations, *Methods Enzymol.*, 2011, **486**, 55–88.

39 A. Punjani, J. L. Rubinstein, D. J. Fleet and M. A. Brubaker, cryoSPARC: algorithms for rapid unsupervised cryo-EM structure determination, *Nat. Methods*, 2017, **14**, 290–296.

40 K. Zhang, Gctf: real-time CTF determination and correction, *J. Struct. Biol.*, 2016, **193**, 1–12.

41 T. Bepler, A. Morin, M. Rapp, J. Brasch, L. Shapiro, A. J. Noble and B. Berger, Positive-unlabeled convolutional neural networks for particle picking in cryo-electron micrographs, *Nat. Methods*, 2019, **16**, 1153–1160.

42 T. Bepler, K. Kelley, A. J. Noble and B. Berger, Topaz-Denoise: general deep denoising models for cryoEM and cryoET, *Nat. Commun.*, 2020, **11**, 5208.

43 A. Punjani, H. Zhang and D. J. Fleet, Non-uniform refinement: adaptive regularization improves single-particle cryo-EM reconstruction, *Nat. Methods*, 2020, **17**, 1214–1221.

44 S. H. Scheres and S. Chen, Prevention of overfitting in cryo-EM structure determination, *Nat. Methods*, 2012, **9**, 853–854.

45 K. Jamali, L. Käll, R. Zhang, A. Brown, D. Kimanius and S. H. W. Scheres, Automated model building and protein identification in cryo-EM maps, *Nature*, 2024, **628**, 450–457.

46 P. Emsley and K. Cowtan, *Coot*: model-building tools for molecular graphics, *Acta Crystallogr., Sect. D:Biol. Crystallogr.*, 2004, **60**, 2126–2132.

47 P. D. Adams, P. V. Afonine, G. Bunkoczi, V. B. Chen, I. W. Davis, N. Echols, J. J. Headd, L. W. Hung, G. J. Kapral, R. W. Grosse-Kunstleve, A. J. McCoy, N. W. Moriarty, R. Oeffner, R. J. Read, D. C. Richardson, J. S. Richardson, T. C. Terwilliger and P. H. Zwart, PHENIX: a comprehensive Python-based system for macromolecular structure solution, *Acta Crystallogr., Sect. D:Biol. Crystallogr.*, 2010, **66**, 213–221.

48 S. Stoll and A. Schweiger, EasySpin, a comprehensive software package for spectral simulation and analysis in EPR, *J. Magn. Reson.*, 2006, **178**, 42–55.